Acta Biomaterialia 125 (2021) 322–332

Contents lists available at ScienceDirect

Acta Biomaterialia

journal homepage: www.elsevier.com/locate/actbio

Full length article

Coaxial micro-extrusion of a calcium phosphate ink with aqueous solvents improves printing stability, structure fidelity and mechanical properties

Romain Bagnol[a,b], Christoph Sprecher[a], Marianna Peroglio[a], Jerome Chevalier[c], Redouan Mahou[d], Philippe Büchler[e], Geoff Richards[a], David Eglin[a,b,*]

[a] AO Research Institute Davos, Clavadelerstrasse 8, 7270 Davos Platz, Switzerland
[b] Department of Biomaterials Science and Technology, Faculty of Science and Technology, University of Twente, Drienerlolaan 5, 7522 NB Enschede, the Netherlands
[c] University of Lyon, INSA-Lyon, CNRS, MATEIS UMR 5510, F-69621, Villeurbanne, France
[d] RegenHU SA, Villaz-Saint-Pierre, Switzerland
[e] ARTORG Center for Biomedical Engineering Research, University of Bern, Bern, Switzerland

ARTICLE INFO

Article history:
Received 11 September 2020
Revised 13 February 2021
Accepted 16 February 2021
Available online 22 February 2021

Keywords:
3D Printing
Calcium phosphate
Printability
Bone substitute

ABSTRACT

Micro-extrusion-based 3D printing of complex geometrical and porous calcium phosphate (CaP) can improve treatment of bone defects through the production of personalized bone substitutes. However, achieving printing and post-printing shape stabilities for the efficient fabrication and application of rapid hardening protocol are still challenging. In this work, the coaxial printing of a self-setting CaP cement with water and ethanol mixtures aiming to increase the ink yield stress upon extrusion and the stability of fabricated structures was explored. Printing height of overhang structure was doubled when aqueous solvents were used and a 2 log increase of the stiffness was achieved post-printing. A standard and fast steam sterilization protocol applied as hardening step on the coaxial printed CaP cement (CPC) ink resulted in constructs with 4 to 5 times higher compressive moduli in comparison to extrusion process in the absence of solvent. This improved mechanical performance is likely due to rapid CPC setting, preventing cracks formation during hardening process. Thus, coaxial micro-extrusion-based 3D printing of a CPC ink with aqueous solvent enhances printability and allows the use of the widespread steam sterilization cycle as a standalone post-processing technique for production of 3D printed personalized CaP bone substitutes.

Statement of significance

Coaxial micro-extrusion-based 3D printing of a self-setting CaP cement with water:ethanol mixtures increased the ink yield stress upon extrusion and the stability of fabricated structures. Printing height of overhang structure was doubled when aqueous solvents were used, and a 2 orders of magnitude log increase of the stiffness was achieved post-printing. A fast hardening step consisting of a standard steam sterilization was applied. Four to 5 times higher compressive moduli was obtained for hardened coaxially printed constructs.

This improved mechanical performance is likely due to rapid CPC setting in the coaxial printing, preventing cracks formation during hardening process.

1. Introduction

Bone defects caused by trauma or diseases are still a leading cause of patient functionality impairment, whether or not the defect has a critical size [1]. Often, synthetic bone substitutes are used to restore anatomy and promote bone ingrowth. Calcium

---

* Corresponding author.
E-mail address: david.eglin@aofoundation.org (D. Eglin).

https://doi.org/10.1016/j.actbio.2021.02.022
1742-7061/

Phosphate (CaP), either as sintered blocks, granules or cements, are the most commonly implanted synthetic bone substitutes [2]. Their similarity to the bone inorganic phase and their osteoconductive nature [3], make them suitable alternative to bone autograft especially in large defects with complex shape. Injectable self-setting Calcium Phosphate Cements (CPCs) are prepared by mixing a reactive CaP powder with a liquid carrier such as water or an organic phase. Setting and hardening occur in contact with an aqueous media upon mixing or diffusion of water in situ [4]. CPCs are very effective in filling complex bone defects compared to granules, but gradients in the CaP setting can occur due to the limited accessibility of the water in the bulk of the cement, leading to heterogeneous structural and mechanical properties [5]. Moreover, there is limited control over the shape and internal architecture of the implanted material. The latter is a critical parameter for vascularization and bone ingrowth and ensued bone defect healing [6].

Extrusion-based printing of a self-setting cement has the potential to allow rapid production of CaP implants with controlled internal macrostructure, but also personalization of synthetic bone grafts fitting patient bone defects, as already demonstrated in several preclinical studies [7–9]. CPCs inks used in micro-extrusion-based 3D printing are mainly formulated on a reactive calcium phosphate (e.g. α-TCP) phase combined or not with others inorganic calcium phosphate particles. A carrier liquid is used to modulate the injectability and the setting time, and is either made of an aqueous medium containing polymers such as alginate, or a non-aqueous organic phase [10–13]. However, there are still challenges related to the efficient production of personalized implants and the development of a fast process, especially required for potential in-hospital manufacturing [14]. A first challenge is to maintain the injectability of the self-setting CaP ink through the cartridge and printing head during the whole printing time. For this purpose, the rheological behavior and setting kinetics of the cement are of paramount importance [15]. This has notably been addressed by using an inorganic liquid as CaP carrier [16,17]. For example, Heinemann *et al.* reported a CPC with a predominantly α-tricalcium phosphate (α-TCP) crystalline phase with lower amount of hydroxyapatite, monetite, calcite and β-TCP dispersed in an organic phase of surfactants and triglycerides insoluble in water [5,18]. The organic phase allows for long-term storage and higher reaction homogeneity. The cement setting is triggered by the exposure to water, dissolution of the α-TCP particles by hydrolysis and reprecipitation as calcium deficient hydroxyapatite (CDHA) [19]. Therefore, water needs to reach and react with the α-TCP for complete setting and hardening.

The second challenge is the shape stability of the printed structure until complete cement setting has occurred. For soft polymeric materials with a viscoelastic behavior such as poloxamer gel, hyaluronan methacryloyl or alginate solutions, collapse and sagging of hanging filaments is often reported [20–23]. Low viscosity hydrocolloids of biopolymer regularly face this problem before a crosslinking step for shape preservation [24]. Pore closure due to adjacent filaments fusion can occur, causing the loss of the implant's internal structure [25,26]. The main forces responsible for these effects are the surface tension which leads filaments to minimize their surface area and the gravity leading to a general loss of structure due to sagging or compression [27]. Minimizing shape deformation can be done by adjusting the viscoelastic properties of the ink and its yield stress. However, this is only possible up to a certain point when using a non-crosslinked viscous phase as extrudability tend to be severely reduced by an increased viscosity. More commonly, support structures are used to stabilize the object during its printing [28]. However, this technique leads to more processing steps, significantly higher printing time, material consumption and economical cost, and it cannot accommodate all shape deformations.

Finally, a 3D printing process that is compatible with hardening protocols as well as sterilization processes is required to open new outlooks for the use of an off-the-shelf CPC ink for rapid production of personalized macro-structured bone substitutes [16]. Indeed, lengthy high-temperature processes are commonly used for sintering CaP ceramics, while CPCs are often hardened by mixing an initial powder with an aqueous solution or by exposing a ready to use cement to an aqueous or humid environment at low temperature. As an example, Raymond *et al.* used an α-TCP/Pluronic F127 ink and exposed the printed scaffolds to a 37°C water biomimetic treatment, a water-immersed 121°C autoclave treatment and a vapor 121°C autoclave treatment [16]. They found that the autoclave treatments significantly decreased the setting times of the scaffolds, but also that the vapor treatment resulted in a different final crystalline phase than the two other treatments, with higher unreacted α-TCP and formed β-TCP proportions, and a lower CDHA proportions. Others have printed successfully scaffolds from α-TCP with polyvinyl alcohol as a sacrificial material or α-TCP/hydroxyl propyl methyl cellulose pastes and used immersion in water at room temperature or 37°C as a hardening process [29,30]. Akkineni *et al.* used an ink with 60 w:w % α-TCP to print and harden scaffolds in a 37°C humidity saturated atmosphere for 3 days [31]. Steam sterilization protocol has already been used for CaP bone substitutes sterilization but is poorly explored as a stand-alone post-processing hardening of 3D-printed CaP ink made of a CPC with an organic carrier liquid.

Therefore, we hypothesized that wetting a self-setting CPC ink with aqueous solvents upon its extrusion from a printing head would trigger rapid setting through hydrolysis, increase the yield stress, and change the filament's surface tension, thus improving shape stability and fidelity, which consequently would improve final structural and mechanical properties of the hardened 3D-printed CaP scaffolds. Contact angle measurements suggested a higher miscibility of water:ethanol mixtures in the CPC ink compared to pure water. Considering the hydrophobic nature of the CPC carrier liquid, we hypothesized that the increased co-solubilization of water:ethanol mixture would increase the water penetration inside the filaments and lead to a faster and more homogeneous setting. While coaxial printing has been used to produce hollow or core-shell ceramic struts to promote scaffold vascularization [32,33] and improve mechanics and osteogenesis [34], to our knowledge it has never been conducted to enhance CPC ink printability and scaffolds post-printing stability.

In this study, a coaxial printing head allowing for pressure driven micro-extrusion of a self-setting CPC ink at the core, and controlled flow of aqueous solvent at the periphery of the extruded central filament is developed. A well-reported and characterized CPC ink is selected to validate the coaxial printing and post-processing with clinically relevant ink [29,31,35–38]. Printability and shape fidelity are assessed by printing an helicoidal structure and measuring the number of printed layers when structure collapse occurs. Mechanical compression tests are performed just after printing. Steam sterilized 3D-printed CaP samples produced using a coaxial printing head in the presence and absence of solvents are characterized by mechanical compression tests, computed tomography, nitrogen sorption, X-ray diffraction and thermogravimetric analyses.

2. Materials and methods

2.1. Self-setting calcium phosphate cement

The calcium phosphate cement ink was provided by RegenHU Ltd (Osteoink^{TM}, Villaz-St-Pierre, Switzerland). The CPC ink is similar to the CE-marked ready-to-use CPC developed by Innotere GmbH (Germany), and is mainly composed of α-tricalcium phosphate (α-TCP) with smaller amounts of hydroxyapatite, monetite, calcite and β-TCP, and a carrier liquid composed of triglycerides and surfactants as previously described [5]. Thermogravimetric analysis of the ink indicated a powder to carrier liquid weight ratio of 4.65 matching closely values reported in literature [5]. Setting of the cement occurs via the hydrolysis of the α-TCP and is controlled by the presence and substitution of the water immiscible organic phase by water. Initial setting time was reported to be of 2.5 min with final setting time of 16 min [5].

2.2. 3D printing

A 3D Discovery Evolution™ Bioprinter (regenHU, Villaz-St-Pierre, Switzerland) was used for all experiments. A custom-made coaxial extrusion head was designed and produced. It consisted of the combination of an outer and inner part, with the inner vessel of the extrusion head having an outlet diameter of 300 µm for the CPC (image of the extrusion head available in Supplementary Figure 1). The outer part was fitted around to leave a ring-shaped gap with an approximate width of 350 µm for the flow of solvent which was coming from a connected 3 mL syringe. The flows of both parts were controlled by a pneumatic pressure system. All samples were printed at room temperature and ambient humidity. Samples were all printed in a row and then post-processed, with post-processing (described below) performed between 6 and 24 h after completing the printing.

A first CAD model used for 3D printing was a cylinder with 6 mm diameter, 3 mm height. The printing followed a 0°/90° layer pattern, 0.858 mm spacing between filaments centers, 0.15 mm between layers and a theoretical porosity of 39% when hypothesizing printing 300 µm diameter filaments. The printing head speed was 3 mm per second and the printing pressures were in a range of 0.139-0.141 MPa for the Osteoink™ and 0.020-0.022 MPa for the solvents. The samples were printed on standard histology glass slides without surface or topography treatments, fixed to the printing platform, with ten samples per glass slide (Gcode_Cylindrical_Model_x10.docx, in Supplementary Material). This CAD design was used to ensure shape equivalence for all groups, but present a suboptimal geometry for compression test, in comparison to recommendation. Mechanical testing, µCT observation and thermogravimetric analysis were performed. For the mechanical tests before steam sterilization, 5 samples per condition were printed. For the mechanical tests after steam sterilization, 16 samples per condition were printed.

For SEM and XRD analyses, a sufficient quantity of material per sample was required (> 500 mg). Therefore, a cuboid structure with a 10 × 10 mm square base and 5 mm height was designed with a 0°/90° layer pattern, a space of 0.667 mm between filament centers and 0.244 mm between layers (Gcode_Square_Model.docx, in Supplementary Material) and printed with identical conditions as the other geometries.

Four different printing conditions were tested. The ink was either printed without solvent (NS), with 50:50 water:ethanol: v:v % (50W), with 75:25 water:ethanol: v:v % (75W) or with demineralized water (100W).

2.3. Steam sterilization (post-processing)

Printed samples were stored at room temperature and ambient humidity for 6 to 24 h maximum before performing post-processing. This latter was conducted in a standard sterilization autoclave (Belimed Infection Control, Belimed Sauter AG, Sulgen, Switzerland) and followed several steps. The glass slides (with the printed samples on top) were first introduced inside a beaker laterally disposed in the autoclave to limit the impact of rapid air and steam movement on the scaffolds structure. Secondly, a 2:30 min vacuum pulse was applied, followed twice by alternating between a 45 s steam pulse and a 2:30 min vacuum pulse. The temperature and steam pressure were then increased to reach 134°C and 3000 mbar and kept at this level for 18 min. Then the steam was expulsed by vacuum and the temperature slowly increased from 65 to 100°C for 30 min while maintaining a vacuum state to dry the samples. Finally, the air was progressively injected to return to the room pressure.

2.4. Post-printing stability

The post-printing stability was tested by printing a helicoidal shape, previously created by the generation of a CAD file (Gcode_Helicoidal_Model.docx, in Supplementary Material). The helicoid was 10 mm diameter, with one filament printed per layer, with an angle shift of 1.432° between each layer (or a lateral shift of 0.125 mm at the extremities of the helicoid), and a vertical distance of 0.15 mm between each layer. The printing process was video recorded until mechanical failure of the construct (e.g. crumbling of the helicoid) occurred; the starting time of the printing and the time of structure failure were used to calculate the number of layers printed before structure failure. The number of samples per condition was 5.

2.5. Contact angle measurement

Flat surfaces were created by depositing and smearing the ink on a glass slide with two glass spacers of 1 mm thickness on the sides. Then, contact angle measurement was performed and recorded using a Krüss DSA10 contact angle instrument (Krüss GmbH, Hamburg, Germany) with 5 µL droplets of MilliQ water, 25 and 50% ethanol. The software ImageJ was used on the acquired images to measure the angle formed by the intersection of the liquid-solid interface of the droplets 10 seconds after their deposition.

2.6. Printing of a human mandibular defect model

The printing of human mandibular defect model was chosen as a proof of concept to evaluate the potential of extrusion coaxial-printing to provide pieces with complex shapes and tailored porosity. A 3D CAD model was extracted from a CT scan of a synthetic bone model of human mandibula with a large defect. The printing path was generated by BioCAM Software (RegenHU Ltd, Villaz-St-Pierre, Switzerland) with a theoretical porosity of 60%. Scaffolds with and without support structures (SS) were generated as controls using a normal extrusion printing process without solvents. The scaffolds printed with solvents were printed without support structure. The printing conditions were optimized for each groups for best shape fidelity. The shape fidelity of the scaffolds was assessed by measuring the deviation of a large overhang (72°) compared to the theoretical model ($N \geq 4$ for all groups except SS with $N=1$) and the internal porosity of the same internal region of the scaffolds measured by µCT and compared to the theoretical porosity (60%).

2.7. Mechanical tests

The mechanical testing protocol was based on previously reported test with a similar ink [38]. To assess the influence of the solvent used on the initial stability of the scaffolds, compression tests before post-processing were performed on an Instron® 5866 machine (Instron, Norwood, USA), with a 100 N load cell and a head speed of 0.2 mm/min until a total displacement of 2 mm was reached. Scaffolds were printed one by one (Gcode_Cylindrical_Model.docx, in Supplementary Material) and tests were always started 10 min after the end of the scaffold's printing to prevent variation in the cement setting time. Five samples were tested per condition.

To assess the influence of the solvent on the final mechanical properties of the scaffolds, compression tests after post-processing were done on the same testing machine, with a 1 kN load cell and a head speed of 0.2 mm/min, until a total displacement of 2 mm was reached. The maximal strength (represented with stress values) and the corresponding strain were measured. When no clear maximum was visible but a clear decrease in slope was observed, the slope transition point was chosen as maximum. As the surfaces of the scaffolds were not perfectly flat for every sample due to manufacturing defects, the start of the measurement reported corresponds to the sample positioning. To avoid errors in the maximal strength corresponding displacement and to start the mechanical curves in the elastic domain of the samples, we corrected the curves by setting the point of displacement 0 at the point where each sample reached 8% of the mean maximum force of its respective group. We decided to use a relative rather than absolute repositioning as the non-linear parts of the curves appeared proportional to the maximal strength of each curve, which was very different between the groups. Eight samples per condition were tested. The curves of each group shown in Fig. 3 were averaged. For a given strain, the stress was calculated as the average of the stress of the other samples at the same strain. The averaged curves were also smoothened, the stress at a given strain was calculated as the mean of the 25 points measured before and the 25 points measured after it in the original curve.

2.8. Micro-computed tomography (CT)

The computed tomography analysis was performed using a vivaCT40 instrument (Scanco Medical AG, Brüttisellen, Switzerland), set at 70 kV energy and 114 µA intensity. Two-dimensional CT images were reconstructed to form 2048 × 2048 pixels matrices from 1000 projections using a cone-beam convolution back projection procedure. Images were saved in 3D-arrays using a 10 µm isotropic voxel size and 10 µm slice increment. For analysis, an identical cylindrical volume was defined for all samples. Grey-value images were segmented using the same threshold value for all samples to distinguish porosity from material. The structural indices of the structures were computed and determined using the analysis method described by Hildebrand [39]. The porosity of the samples was calculated using the BV/TV (the % of material volume relative to total volume) and corresponded to 1- BV/TV. The average material thickness was calculated using Tb.Th* (trabecular thickness or material thickness) and the average porosity size using Tb.Sp* (trabecular separation). Three samples were analyzed per group, and the values reported are the average values. The criteria used to judge the quality of a construct were the presence or absence of cracks, porosity within the filaments and broken parts.

2.9. Nitrogen sorption

N_2 adsorption–desorption analysis was performed on post-processed samples using a Micromeritics ASAP 2020 (Instrument Corp., Norcross, USA). Around 1 g of sample equivalent to 5-6 combined cylindrical printed scaffolds was degassed under vacuum at 25°C for at least 24 h prior to analysis. The specific surface area (SSA) and the desorption average pore width (4V/A by BET) values were determined using the Brunauer–Emmett–Teller (BET) theory.

2.10. X-ray diffraction (XRD)

The crystalline phase composition analysis was conducted on a D8 ADVANCE (Bruker AXS GmbH, Karlsruhe, Germany) with Bragg-Brentano geometry equipped with a germanium monochromator using a CuKα Ni-Filter. A scan range of 4-60 °2θ, a 0.25 sec time per step with a 0.0122 °2 θ step size was used. The Rietveld Refinement method was performed for quantification of crystalline phases contents and the hydroxyapatite crystallite size average values following the Debye-Scherrer method using BGMN 4.2.22 software [40]. The following samples were analyzed: the pristine ink and the coaxial printed structures with the different conditions.

2.11. Scanning electron microscopy (SEM)

Scanning Electron microscope observations were conducted using a field emission Hitachi S-4700 II microscope (Hitachi Ltd, Tokyo, Japan). The microscope parameters were adjusted for each measurement, however a working distance in the range of [5.3 – 15.9 mm], an acceleration voltage in the range of [1 kV – 10 kV] and an intensity in the range of [15.5 – 48 µA] were used. Before observation, a 10 nm carbon layer was deposited on the samples by using a Bal-Tec CED030 coater (Bal-Tec, Balzers, Liechtenstein).

2.12. Thermogravimetric analysis (TGA)

The instrument used for the thermogravimetric analysis was a Thermogravimetric Analyzer TG 209 F1 (NETZSCH GmbH, Graz, Austria). Measurements were performed between 30 and 550°C in an oxygen (quality 2.5) saturated chamber with a heating rate of 10°C/min. The obtained weight loss curves were then used to determine the amount of organic phase contained in the samples. It was assumed that only traces of water were still present in the scaffolds, and that the organic phase will be evaporated or degraded in the range of temperature used. Samples were prepared by using the crushed samples remaining from the mechanical testing after post-processing. A scalpel was used to isolate several small fragments and the total mass was at least 100 mg for each measurement. The samples were not further crushed into powder with a mortar to minimize the mechanical separation of the organic and inorganic phases altering the measurement. Three post-processed samples were tested by conditions. For the fresh ink group, measurement was performed in quadruplicate on a fresh unopened cartridge.

2.13. Statistical analyses

Statistical analyses were performed using GraphPad Prism version 8.1.0 for Windows (GraphPad Software, La Jolla, California, USA). Normality of each separate set of data was tested. In case of normality, such as for the Max Strength (N=8) and Slope (N=8) values, an ANOVA test was applied. If statistical difference was found, a Tukey's multiple comparison test was applied ($p < 0.05$). For all the other data sets with non-normal distribution, Thermogravimetric analysis (N=3), Contact Angle (N=5), Post-printing stability (N=4), Slope measured after printing (N=5), Stress at 12% strain measured after printing (N=5), Scaffolds weight after post-processing (N=7 for NS, N=8 for other groups), Strain at Max Stress (N=8), Scaffolds porosity (N=3), Scaffolds trabecular size (N=3), Scaffolds porosity size (N=3), Mandibular defect overhang (N>4) a Kruskal-Wallis test was applied. If statistical difference was found, a non-parametrical Dunn's comparison test was applied and statistical significance assessed at $p<0.05$. Two-tailed Pearson and Spearman correlation tests were used to evaluate the correlation between the maximum stress and density of the 6mm diameter*3mm height scaffolds.

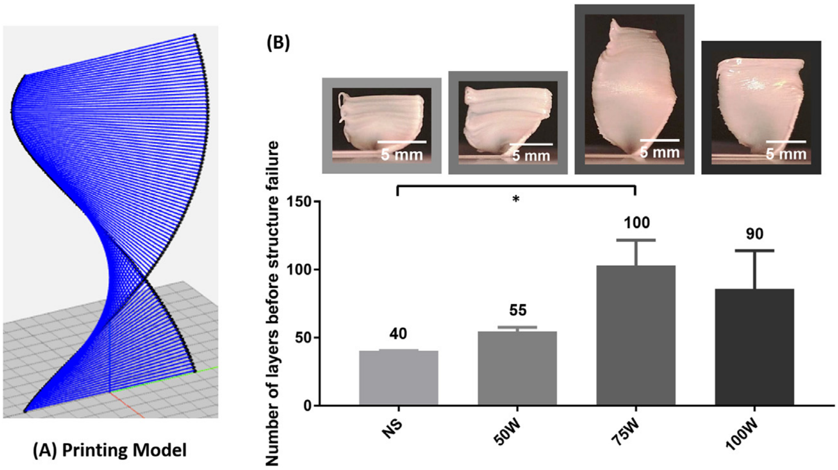

Fig. 1. (a) CAD design of the helicoidal model to assess printability of CaP cement. (b) number of layers before failure for structures-built NS, 50W, 75W and 100W in the coaxial printing, with representative images of printed helicoidal structures just before collapse.

3. Results

3.1. Post-printing stability of self-setting CaP cement is improved by coaxial extrusion with water-containing solvent

First, the ink surface tension and affinity of solvent to the cement surfaces as measured by contact angle shows a decrease in contact angle values with decreasing water:ethanol volume ratio, 28° ± 1°, and 24° ± 5° and 16° ± 3° respectively for 100W, 75W and 50W ($100W > 50W = p < 0.05$).

Then, the number of layers of the helicoidal structure printed before failure for all tested groups as well as representative images of printed helices are reported in Fig. 1. For one sample of the 75W group, the structure did not fall after reaching the maximum of 127 layers in the G-code file. Hence, we decided to exclude the highest layer number for each group to ensure an equal number of 4 samples per condition. The highest number of layers before collapse of the structure is achieved for the coaxial extrusion with 75W, followed by 100W, 50W and finally NS ($75W > NS = p < 0.05$). Interestingly, the standard deviation is the highest for the 100W group, followed by 75W, then 50W and NS group for which the number of layers before failure is very consistent and the standard deviation low. More sagging is observed for the NS group and the 50W group compared to the 75W and 100W groups. The groups also show differences in their structure failure mechanism. Indeed, for the NS and 50W groups an overall bending of the structure is observed when it fails. For the 75W and 100W groups, the bending is often concentrated on a few layers, creating visible separations between filaments indicating a failure at their junction. In the 100W condition, the filaments are slightly dragged up when the printer head finishes printing a filament and goes up for the following layer, showing that the adhesion between filaments is lower than in the other groups. Compared to the NS group, coaxial printing with solvents allows creation of structures with a higher number of printed layers, with a 1.3-, 2.5- and 2.1-folds increase of layers for the 50W, 75W and 100W groups, respectively.

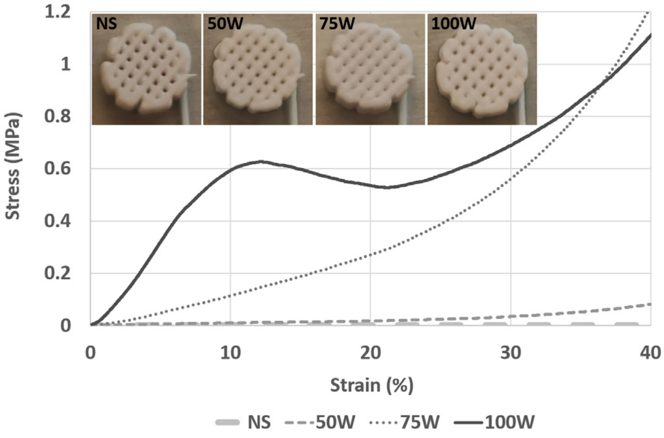

Fig. 2. Representative images of the samples before mechanical testing and averaged (N= 5 Samples/group) stress / strain compression curves of coaxial 3D Printed self-setting CaP cement scaffolds before post-processing (NS, 50W, 75W and 100W).

3.2. Coaxial extrusion of self-setting cement with water containing solvent induces rapid setting of the cement and improves mechanical stability of printed structures prior to post-processing

In a following experiment, cylindrical microporous scaffolds were printed, and their compressive properties tested 10 minutes after the end of the printing process (Fig. 2). The stiffness was calculated based on the linear part of the strain-stress curves, which was defined as the points between 2 and 6% of strain for each sample. The NS group shows very low stiffness, with a slope value of 6.4 ± 0.6 kPa ($100W$ and $75W > NS = p < 0.05$), suggesting an almost pure viscous behavior with no significant cement setting during the printing and the time of the test. The 50W group has a slope value of 90 ± 10 kPa ($100W > 50W = p < 0.05$), which then increases after 20% strain. The 75W group shows significantly higher stiffness, mostly linear from 0 to 20% strain with a slope value of 1.3 ± 0.5 MPa ($75W > NS = p < 0.05$), followed by an exponential increase in stress from 20 to 40% strain. Both the 50W and 75W groups show a low initial stiffness, followed by a gradual shift from a linear to an exponential increase of stress in response to strain, suggesting compaction rather than a ductile behavior. The 100W condition shows first the highest stiffness of the tested groups, with a slope value of 7.5 ± 0.9 MPa ($100W > NS$ and $50W = p < 0.05$), reaching a maximum around 12% strain. Then, it is followed by a slight decrease in stress until 21% strain, and an increase with an exponential tendency from 21 to 40% strain. It is the only group showing a ductile behavior, which is then followed by compaction. As a maximal strength measurement was not possible for all the groups, the stress at 12% strain - where the 100W condition reaches a maximum - was instead measured for every curve. Indeed, the nature of the solvent used has a large impact on the stress measured at 12% strain. The average value measured

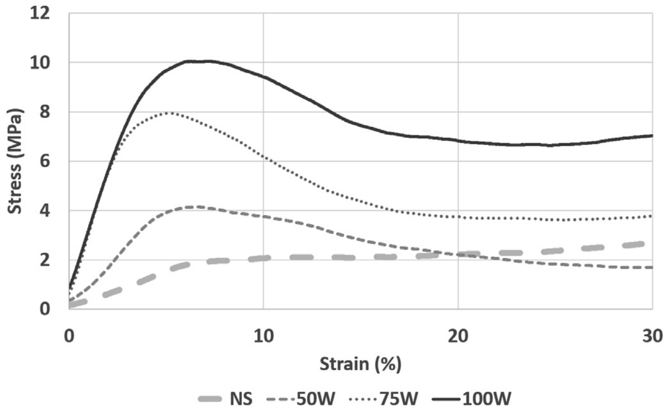

Fig. 3. Average compression curves of coaxial 3D printed CaP scaffolds after post-processing (NS, 50W, 75W and 100W).

is 0.9 ± 0.1 kPa for the NS group (NS $<$ 75W and 100W = $p < 0.05$), 12 ± 3 kPa for the 50W group (50W $<$ 100W = $p < 0.05$), 150 ± 40 kPa for the 75W group (NS $<$ 75W = $p < 0.05$) and 600 ± 100 kPa for the 100W group (NS and 50W $<$ 100W = $p < 0.05$). In comparison to the NS group, a 13-, 170- and 700-fold increase respectively for the 50W, 75W and 100W conditions are measured.

3.3. Coaxial extrusion of self-setting cement with water containing solvent improves mechanical properties of printed structures post-processing

The averaged compression curves of the printed scaffolds after post-processing (sterilization) are reported in Fig. 3. For the 3 groups using coaxial liquid, a clear maximum stress is visible on all curves. The maximum stress and corresponding strain are calculated from the raw data, using a mathematical function to find the point with the highest stress in an interval of points around the maximum. For these 3 groups, an increase of the stress value is observed with the strain in a quasi-linear way until a maximum is reached between 5-8% strains. Then, the stress decreases as the strain increases until a plateau is reached at around 15-20% strain. A further increase of stress is observed at higher strain, above 30%, attributed to compaction of the CaP cement. For the group NS, the maximum stress is not clearly visible, and a transition from a linear increase of the stress to a less steep linear increase is usually seen. In these cases, the end of the transition between the two slopes is manually chosen, then the same mathematical function mentioned before is used to find the maximum stress and corresponding strain between the start of the assay and the point picked manually. For the NS group, a quasi-linear increase of the stress is observed with a steeper increase up to 6% strain, followed by slower increase up to 40% strain.

The values of the maximal compression strength, the corresponding strain, the slope in the linear part of the curve and the weight of the scaffolds are reported in Table 1. The use of solvents in the coaxial extrusion process influences the maximal compression strength of the post-processed CaP scaffolds. The maximal compression strength value of the 100W group is significantly higher than the 75W, 50W and NS group. Compared to the NS group, the maximal strength is approximately 2.2, 4.6 and 5.2 folds higher respectively for the 50W, 75W and 100W groups. All scaffolds have similar strain at the maximal strength; however, it is slightly lower for 75W. The slopes were calculated using the points between 20% and 80% of the maximum stress as it appeared to be the range with the most linear increase. The values of the slope are the highest for the 75W group, closely followed by the 100W group, then significantly lower for 50W and NS. The weights of the scaffolds are not significantly different between the 50W, 75W and 100W, and slightly, but significantly higher than for the NS group.

3.4. The structural integrity and shape fidelity of the CaP scaffolds post-processing depends on the use of water containing solvent

The coaxial 3D printed CaP scaffolds after post-processing were imaged using CT analysis to characterize their internal macrostructure and the presence of defects, and cracks (Fig. 4 and Table 2).

The scaffolds from the 100W condition show the least structural defects and the best overall structure conservation, without cracks or significant intra-filament porosity or broken parts. The scaffolds from the 75W present some small cracks on the edges, but no significant intra-filament porosity or broken parts. The scaffolds in the 50W group have more defects, with cracks and intra-filament porosity throughout the scaffolds. The scaffolds of the group NS present the worst structure integrity, with large cracks and intra-filament porosity as well as large broken sections (8/16 printed structures). Side views and information about scaffolds dimensions are given in Supplementary Figure S3. Table 2 summarizes several macrostructural characteristics of the printed scaffolds after post-processing analyzed by µCT.

The overall macroporosity value is the highest for the NS scaffold, followed by 100W, 50W and 75W scaffolds. The trabecular size average values are not significantly different for the 3 scaffold groups using coaxial solvent, but higher than the value for the NS scaffolds. The pores size average value measured by CT is the highest for the NS scaffolds, followed by 100W, 50W and 75W. SEM observations of the different scaffolds' non-fractured surfaces present a similar granular aspect, even at higher magnification, with needle-like structure rarely observed (Supplementary Figure S2). Fractured surfaces from all groups are similar with no obvious differences in surface aspect or size of crystals (Supplementary Figure S2).

The influence of the coaxial micro-extrusion-based 3D printing on the structural reproducibility of a theoretical design was further assessed using a mandibular defect model (Figs. 5 and 6).

The NS experimental overhang shows a deviation of 10° from the theoretical angle while the SS group presents a minimal deviation as expected. The 100W angle difference value is 16°, while the 75W and 50W angle difference are not significantly different from SS group value.

The NS group porosity value of 40% deviates by 20% from the theoretical porosity. The 100W and 75W groups have an experimental porosity around 45%, while the 50W group porosity value is the closest to the planned design.

3.5. The coaxial 3D printing of the self-setting CaP cement with water containing solvent does not impact significantly the microstructure, crystalline composition and crystalline phases after post-processing

Nitrogen sorption analysis was performed to further assess the surface nano- and meso-porosity of the post-processed scaffolds (Table 3 and Fig. 7).

The calculated SSA and the desorption average pore width values are almost identical for all samples with a trend toward an increase of surface area with increased water amount in the coaxial printing process (Table 3).

The adsorption desorption isotherm profiles are identical for all samples (Fig. 7). They can be described as type III isotherm, and they display a H3 hysteresis loop according to the IUPAC classification [41]. Similar isotherms have been reported for CPC surfaces with aggregated plate-like particles containing slit-shaped pores, albeit with higher SSA [42,43].

Table 1
List of average and standard deviation values of the maximum strength (measured by stress), strain at maximum strength, slope and weight of coaxial 3D printed CaP scaffolds after post-processing (NS, 50W, 75W and 100W).

Group	NS	50W	75W	100W
Maximum Strength (MPa)	2 ± 0.3 (*,**,***)	4.5 ± 0.4 (***,###)	9.3 ± 0.9 (**,#,##)	10.5 ± 0.8 (*,##,###)
Strain at Maximum Stress (%)	7 ± 1	7 ± 2	6 ± 1	7 ± 1
Slope in linear regime (MPa)	31 ± 7 (*,**,***)	100 ± 20 (***,###)	230 ± 20 (**,#)	220 ± 30 (*,###)
Weight (g)	0.176 ± 0.007	0.180 ± 0.01	0.189 ± 0.008	0.183 ± 0.007

$P<0.05$ *NS vs 100W, **NS vs 75W, ***NS vs 50W, #50W vs 75W, ##75W vs 100W, ###100W vs 50W

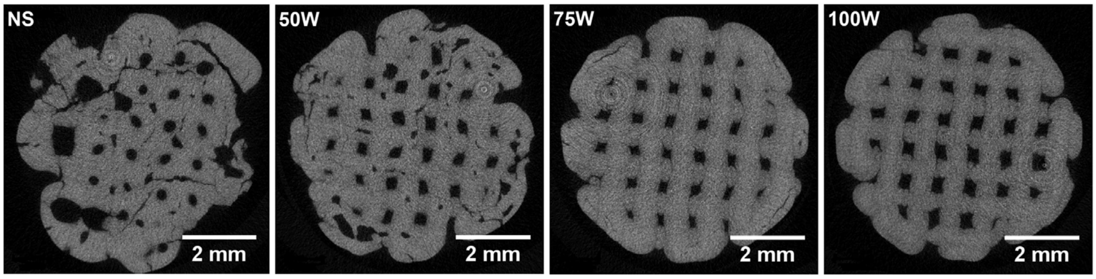

Fig. 4. Representative internal section X-ray images of the coaxial 3D printed scaffolds (NS, 50W, 75W, 100W) after post-processing.

Table 2
List of average and standard deviation values of the porosity, the trabecular size and the pores size of the coaxial 3D printed scaffolds (NS, 50W, 75W and 100W) after post-processing.

Composition	NS	50W	75W	100W
Porosity (%)	18 ± 3	10 ± 4	8 ± 3	13 ± 5
Trabecular Size (mm)	0.46 ± 0.01	0.57 ± 0.06	0.58 ± 0.04	0.58 ± 0.04
Pores Size (mm)	0.23 ± 0.03	0.18 ± 0.4	0.15 ± 0.05	0.21 ± 0.04

$P<0.05$ *NS vs 100W, **NS vs 75W, ***NS vs 50W, #50W vs 75W, ##75W vs 100W, ###100W vs 50W.

Table 3
List of specific surface area (SSA) and desorption average pore width values of the coaxial 3D printed scaffolds (NS, 50W, 75W and 100W) after post-processing.

Composition	NS	50W	75W	100W
SSA (m^2/g)	1.06	1.30	1.82	1.80
Desorption average pore width (nm)	10.5	8.6	9.4	12.6

The crystalline composition and crystalline phases analyzed by XRD following post-processing are reported in Fig. 8, together with the self-setting CaP cement prior to processing as reference sample.

As expected, a change of the crystalline phase composition of the self-setting CaP cement after the post-processing is observed. The CPC ink contains 54.3% of α-TCP, 27.1% of monetite, 9.8% of calcite, 7.5% of hydroxyapatite and 1.3% of β-TCP in mole. After the post-processing, a large increase in the hydroxyapatite or CDHA content, between 36.7% and 42.6% is observed for the different groups. A concomitant decrease of α-TCP content, between 36.4% and 40.1%, monetite content, between 13.8 and 15.1%, and calcite content, between 4% and 4.7%, are measured independently of the conditions used. Furthermore, the calculated hydroxyapatite crystallite average size values are not significantly different between printed groups for both the 001 plane, with a crystallite size of around 40 nm, and the 100 plane, with a crystallite size of around 15 nm. For the fresh CPC ink containing hydroxyapatite particles, the hydroxyapatite crystallite size values measured are slightly higher than the post-processed groups, 57.0 and 17.5 nm for the 001 and 100 planes respectively. It can be safely hypothesized that the measured mean crystallites size after printing reflects the re-precipitation of new and more numerous smaller hydroxyapatite crystallites during the CPC setting post-processing, leading to a mean reduction of the crystallites size. The lack of difference between post-processed groups indicates that the coaxial printing process does not influence significantly the crystallites growth.

3.6. The inorganic and organic contents in the post-processed scaffolds are independent of the manufacturing process

The Fig. 9 shows the averaged curves of the mass loss analyzed by thermogravimetric analysis for the different groups.

The 4 groups have a very similar mass loss curve. First, there is a slow loss of mass from 30 to 230°C, where approximately 2%

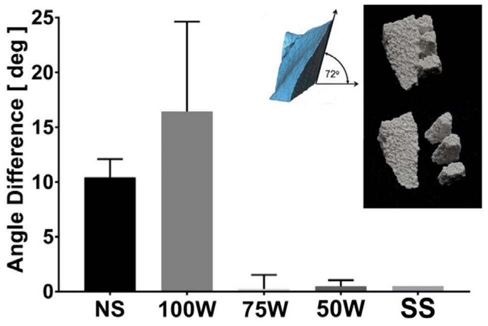

Fig. 5. Plot of the angle difference (Experimental overhang value –72°) for the 3D printed mandibular defect scaffold groups (Insert: theoretical mandibular defect reconstruction and representative images of a 3D printed sample with support structures before and after removal).

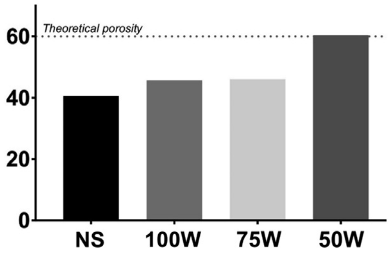

Fig. 6. Plot of the 3D printed mandibular defect scaffold groups porosity measured by µCT (dotted line = theoretical porosity).

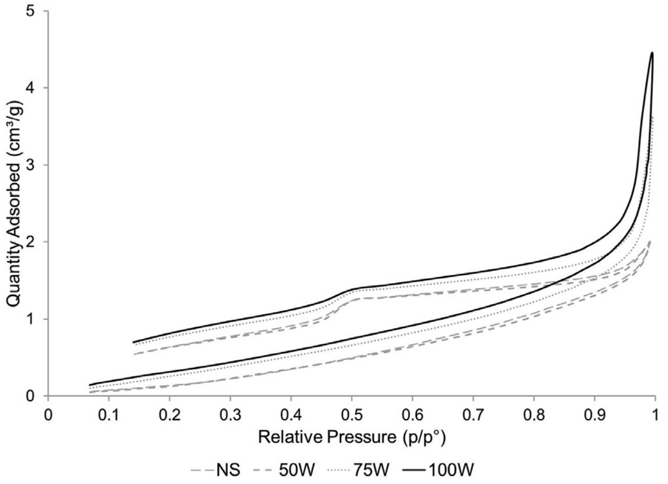

Fig. 7. Nitrogen adsorption–desorption isotherms of coaxial 3D printed scaffolds after post-processing (NS, 50W, 75W and 100W).

of the total sample mass is lost with no significant differences between samples indicating that the co-extrusion with solvents does not influence absorption of weak bond water molecules on post-processed samples. Between 230 and 330°C, the mass loss accelerates with a loss attaining between 13% and 15% of the total mass at 330°C depending on the groups. The slight variation of profiles may be indicative of how the residual organic components in the ink are evaporating and degrading in relation to the organic phase and structure cohesion. Between 330 and 530°C, further mass loss is approximately 2%. At the end of the analysis, the average total mass loss values are very similar, 16, 16, 15 and 17% respectively for NS, 50W, 75W and 100W.

4. Discussion

The self-setting CPC ink used in this work was previously described [5]. The organic phase in which the reactive α-TCP is dispersed, allows for long-term storage, ease of usage for print (no printing time window) and high reaction homogeneity upon exposure to water, causing dissolution of the α-TCP particles by hydrolysis and their reprecipitation as CDHA [19]. Ahlfeld *et al.* successfully reconstructed and printed a scaphoid bone model by combining the ink used in this study with a plasma-alginate-methylcellulose and also created complex structures using a sacrificial soluble methylcellulose support ink [39,44]. Removal and washing out of the sacrificial ink supporting overhanging and cre-

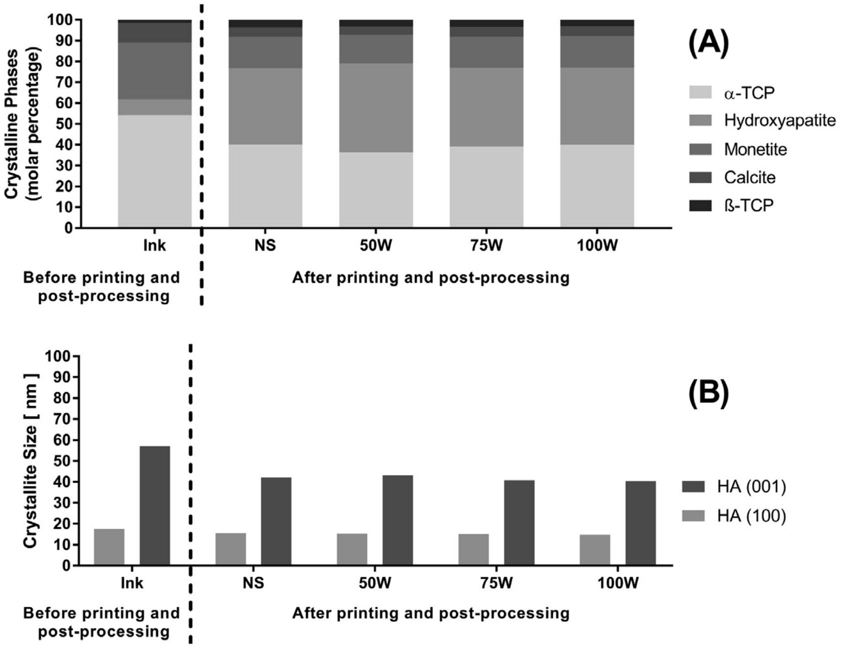

Fig. 8. Plots of (A) the molar % of the crystalline phases measured by molar percentage and (B) the hydroxyapatite crystallite size for the planes (001) and (100) as a function of the coaxial 3D printed scaffolds groups (NS, 50W, 75W, 100W) after post-processing and the self-setting CaP cement before printing and post-processing.

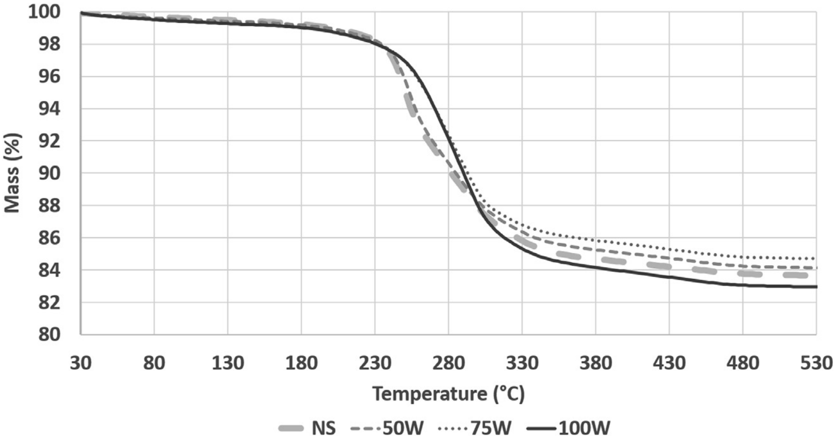

Fig. 9. Plot of the average mass loss of the coaxial 3D printed scaffolds groups (NS, 50W, 75W and 100W) after post-processing as a function of the temperature.

ating hollow structures was required. In another study, this ink was used to create 3D printed CaP scaffolds, which supported bone formation in a rat segmental bone defect [36]. However, a sacrificial structure was also necessary to support overhanging structures.

In order to control the setting reaction of the cement upon extrusion of the ink filament, water and water:ethanol solutions were assessed as reactive coaxial extruded solvents. Contact angle measurements suggested the higher miscibility of water:ethanol with the organic phase in comparison to water alone. It was hypothesized that the water will trigger the hydrolysis starting from the CPC filament surface due to the hydrophobic oil content, while the water:ethanol mixtures will have better co-solubilization and enhance the water penetration inside the struts and induce a faster setting.

Coaxial printing with aqueous solvents resulted in an increased post-printing stability which is beneficial to produce personalized implants without needing support structures.

The results from the helicoidal and the mandibular models further demonstrate the interest of coaxial printing for production of complex structures. As expected, the NS group shows a significant angle difference and low preservation of the theoretical porosity; while the SS group low angle difference matched the CAD design. The 100W large angle difference and reduced porosity are attributed to the decrease in filament adhesion and structural stability as observed for the helicoidal experiment. The use of ethanol and water mixture in the coaxial groups, 75W and 50W, improved the design fidelity with a best result for the 50W for the model and conditions tested. A balance between filament pre-hardening and filament adhesion mediated by the solvents is critical for best shape fidelity prior and post-processing. When assessing the printability and stability of the self-setting CaP cement extruded through a coaxial cartridge with aqueous solvents into a helicoidal structure, higher structural stability was achieved upon printing with 100W and 75W. This was correlated with increased mechanical properties shortly after printing for all the groups using a coaxial liquid, with the 100W group, followed by the 75W achieving the highest increase of mechanical properties. These findings correlate well with observations of Heinemann *et al.* [5] reporting initial and final setting times of 2.5 and 16 min for a similar formulation, suggesting that the rapid setting and yield stress increase of the cement induced upon extrusion from the coaxial head is the main mechanism for improving the printability and shape retention of the structure. Another possible mechanism could be a change in capillary forces inside the filaments induced by the wetting upon coaxial extrusion leading to the increase of viscosity of particles suspensions as reported by Koos *et al.* [45]. A suspension containing particles and a primary carrier liquid can experience a large increase in viscosity via the addition of a small amount of a secondary immiscible liquid. This effect was observed with a suspension of calcium carbonate in diisononyl phthalate with as little as 0.2% addition of water. Given the low miscibility of the components of the organic phase in water for the CaP cement used, this phenomenon could take place. However, the presence of surfactants in the carrier liquid of the used ink formulation would weaken this effect [46]. Hence, capillary forces are unlikely to play a major role.

Overall, a positive influence of coaxial extrusion with an aqueous solvent on the self-setting CPC ink printability was observed. However, wetting of the filaments with water decreased the adhesion between the filaments shortly after printing, leading to struts slippage, especially when printing overhang structures with incomplete overlay of the printed struts. This is likely responsible for the increasing standard deviation observed when printing overhang structures with solvents with increasing water fraction (Fig. 1). On the other hand, a too high ethanol content reduced the setting speed during the printing process. An optimal printability in term of structural and mechanical stability was found for the 75W condition. Both printing of the mandibular defect and the helicoidal structure suggest the need of a balance between filament hardening and filament adhesion, and that this balance could vary depending on the structure printed. The sacrificial support ink method proposed by Ahlfed *et al.* is likely less prone to the creation of structural defects during printing, but requires additional printing and support ink removal times [44].

Steam autoclave post-processing is potentially compatible with clinical needs. In our case, the use of an autoclave cycle as post-processing has the advantage of offering simultaneously a fast setting method and sterilization for coaxially printed samples suggesting the possibility to delocalize manufacturing in non-specialized locations like in the hospital.

Coaxial micro-extrusion with solvents increased the structural integrity and final mechanical properties of the printed CaP scaffolds. After post-processing, only 50% of the NS samples conserved their shape and were therefore mechanically tested. For the other groups, the visual observation of cracks and the percentage of defect samples decreased with the increase of water volume fraction in the solvent. The initial setting and associated mechanical stability of the structures when printed with aqueous liquids is a likely reason for the damage reduction caused by the rapid temperature ramps and steam flow during the sterilization cycle. A relevant comparison can be made with the study from Richter *et al.*, using a CPC ink with a very close composition in which printed structure are post-processed in a 37°C water saturated atmosphere for 3 days, followed by 7 days setting in deionized water [37].

While the geometry and printing conditions used differ slightly, similar scaffolds compressive strengths were obtained while using a post-processing of one hour instead of 10 days. It is known that the cements should not be deformed between the initial and final setting times to avoid the apparition of cracks [47], reported for example in this study [31], and therefore a more complete setting should improve structural integrity . It may be also possible that structure deformation could have been triggered by an increase in the volume of the remaining organic phase coupled with a decrease in viscosity as temperature rises during post-processing resulting in apparition of cracks. Noureddini *et al*. reported the change in density [48] and viscosity [49] of various fatty acids with temperature. They found that both decreased as temperature increased. For the capric acid fatty acid used in these studies, at 37.8°C its viscosity is 6.33 $mPa.s^{-1}$ and its density 0.8863, while at 110°C they respectively lowered to 1.60 $mPa.s^{-1}$ and 0.8332. Interestingly, the remaining amount of organic phase and the crystalline phase transformation as assessed by TGA and XRD were very similar through-out the groups tested after post-processing. Thus, the pre-setting induced by the coaxial printing with water containing solvents may limit the potential impact of the volumetric change of the organic phase. In another study, a CaP cement combined with an alginate/methylcellulose bioink to create biphasic scaffolds, exposed to humidity at 37°C, followed by 10 min bath in a $CaCl_2$ solution and a 3 days incubation in culture medium has been reported to have increased mechanical properties and reduced crack formation [38]. This confirms again that adequate pre-setting is beneficial to preserve structural integrity and final mechanical properties. Conversely, there was no obvious relationship between the water volume fraction in the coaxial liquid used and the samples structural characteristics assessed by CT. The measured average trabecular size or wall thickness was the only structural parameter with significant variations between printed groups with solvents, versus NS. Thus, no obvious correlation exists between organic phase content and mechanical properties. The fast hydrothermal-vapor hardening process used in this study is harsher than the one reported by Raymond *et al.*, higher temperature and pressure [16]. Interestingly, a similar retention of the organic binder is observed in the hydrothermal-vapor, with similar granular surface aspect and SSA value of 2.3 $m^2.g^{-1}$ [16]. It is known that macro and micro-porosity have a negative effect on CaP scaffolds strength [50]. The densities of the mechanically tested scaffolds were calculated and associated to their maximal compressive strength and a mild correlation between the two factors was established both through a Pearson test (R=0.5810, 95% confidence interval [0.3165;0.7616]) and Spearman test (R=0.5198, 95% confidence interval [0.2261;0.7269]). The small increase of N_2 sorption SSA values with the water volume fraction indicated an increase in nanoporosity. However, these small variations cannot explain the large differences observed in mechanical properties. Therefore, the reduction of structural defects created during the post-processing, such as large pores and cracks, is the probable reason for the observed improved mechanical properties [51].

Several limitations can be attributed to this study. 3D printed implants produced with the same CPC used in this study have been assessed in preclinical studies [3,52–54], however the influence of the micro-extrusion and the hardening protocols on the CPC structure degradation has not been reported. A following study is therefore required to assess *in vitro* acellular and cellular resorption behavior to infer implant ageing *in vivo* [55]. Despite steam autoclave being a faster process, a limitation compared to ambient temperature setting is its inability to be used for scaffolds containing heat sensitive biological agents such as cells, growth factors or proteins as they would be destroyed or denatured. Finally, this study was conducted on a commercial CPC ink. However, the co-axial micro-extrusion-based 3D printing and fast hardening optimization of the CPC ink used in this study can be applied to others non-aqueous or aqueous-based CPC inks to improve shape fidelity and resistance to harsh post-processing by similarly modulating the dissolution-precipitation reaction [56]. For example, a following proof of concept could consist in co-extrusion of an aqueous CPC formulation with a disodium phosphate containing solution.

5. Conclusion

Printing and post-printing shape stability is of paramount importance for the development of geometrically complex and porous personalized implants. In this work, we investigated the coaxial micro-extrusion of a self-setting calcium phosphate cement with water:ethanol mixtures to increase the post-printing stability of complex structures, reducing the need of support structures and reducing cost and time of production. Additionally, the initiation of cement setting with water upon coaxial micro-extrusion, rather than with in the ink or post printing, positively impacted the ability to produce 3D printed structures with higher height than normal micro-extrusion. The produced structures could withstand a relatively harsh and fast hardening process based on a standard steam sterilization protocol, achieving conservation of its architectural integrity and improved mechanical properties. The reported coaxial micro-extrusion of CPC ink with water-based solvents removes some of the barriers toward in-hospital fast manufacturing production 3D printed personalized CaP bone substitutes.

Declaration of Competing Interest

The authors declare that they have no known competing financial interests or personal relationships that could have appeared to influence the work reported in this paper.

The authors declare the following financial interests/personal relationships which may be considered as potential competing interests.

Acknowledgments

This work was supported by the Innosuisse grant number 18060 and the AO Foundation. The Graubünden Innovationsstiftung is also acknowledged for its financial support. The authors thank Dr. Nicola Döbelin at RMS Foundation, Bettlach, for performing the XRD analyses. Dr. Karen Mys and Dr. Olivier Ligier are also acknowledged for support in the CT data interpretation and clinical perspective, respectively.

Supplementary materials

Supplementary material associated with this article can be found, in the online version, at doi:10.1016/j.actbio.2021.02.022.

References

[1] A. Nauth, E. Schemitsch, B. Norris, Z. Nollin, J.T. Watson, Critical-size bone defects: is there a consensus for diagnosis and treatment? J. Orthop. Trauma 32 (Suppl 1) (2018) S7–S11.
[2] V. Campana, G. Milano, E. Pagano, M. Barba, C. Cicione, G. Salonna, W. Lattanzi, G. Logroscino, Bone substitutes in orthopaedic surgery: from basic science to clinical practice, J. Mater. Sci. Mater. Med. 25 (10) (2014) 2445–2461.
[3] P.V. Giannoudis, H. Dinopoulos, E. Tsiridis, Bone substitutes: an update, Injury 36 (Suppl 3) (2005) S20–S27.
[4] M.P. Ginebra, M. Espanol, E.B. Montufar, R.A. Perez, G. Mestres, New processing approaches in calcium phosphate cements and their applications in regenerative medicine, Acta Biomater. 6 (8) (2010) 2863–2873.
[5] S. Heinemann, S. Rossler, M. Lemm, M. Ruhnow, B. Nies, Properties of injectable ready-to-use calcium phosphate cement based on water-immiscible liquid, Acta Biomater. 9 (4) (2013) 6199–6207.
[6] T. Genova, L. Munaron, S. Carossa, F. Mussano, Overcoming physical constraints in bone engineering: 'the importance of being vascularized', J. Biomater. Appl. 30 (7) (2016) 940–951.

[7] Y. Zhang, L. Xia, D. Zhai, M. Shi, Y. Luo, C. Feng, B. Fang, J. Yin, J. Chang, C. Wu, Mesoporous bioactive glass nanolayer-functionalized 3D-printed scaffolds for accelerating osteogenesis and angiogenesis, Nanoscale 7 (45) (2015) 19207–19221.
[8] B. Barboni, C. Mangano, L. Valbonetti, G. Marruchella, P. Berardinelli, A. Martelli, A. Muttini, A. Mauro, R. Bedini, M. Turriani, R. Pecci, D. Nardinocchi, V.L. Zizzari, S. Tete, A. Piattelli, M. Mattiol, Synthetic bone substitute engineered with amniotic epithelial cells enhances bone regeneration after maxillary sinus augmentation, PLoS ONE 8 (5) (2013) e63256.
[9] J. Wang, M. Yang, Y. Zhu, L. Wang, A.P. Tomsia, C. Mao, Phage nanofibers induce vascularized osteogenesis in 3D printed bone scaffolds, Adv. Mater. 26 (2014) 4961–4966.
[10] E. Vorndran, M. Klarner, U. Klammert, L.M. Grover, S. Patel, J.E Barralet, Gbureck 3D powder printing of β-tricalcium phosphate ceramics using different strategies, Adv. Eng. Mater. 10 (12) (2008) B67–B71.
[11] R. Trombetta, J.A. Inzana, E.M. Schwarz, S.L. Kates, H.A. Awad, 3D printing of calcium phosphate ceramics for bone tissue engineering and drug delivery, Ann. Biomed. Eng. 45 (1) (2017) 23–44.
[12] A.V Mironov, O.A Mironova, A.O. Mariyanats, V.S Komlev, I.V Smirnov, E.Y. Kananykhina, T.K. Fatkhudinov, V.K Popov, Highly filled compositions based on alginate gel and fine tricalcium phosphate for 3D printing of tissue-engineered matrices, Inorg. Mater.: Appl. Res. 11 (5) (2020) 1137–1143.
[13] J. Franco, P. Hunger, M.E Launey, A.P. Tomsia, E. Saiz, Direct write assembly of calcium phosphate scaffolds using a water-based hydrogel, Acta Biomater. 6 (1) (2010) 218–228.
[14] E. Lanzarone, S. Marconi, M. Conti, F. Auricchio, I. Fassi, F. Modica, C. Pagano, G. Pourabdollahian, in: Hospital Factory for Manufacturing Customised, Patient-Specific 3D Anatomo-Functional Models and Prostheses, Factories of the Future, Springer, Cham, 2019, pp. 233–254.
[15] S. Kyle, Z.M. Jessop, A. Al-Sabah, I.S. Whitaker, 'Printability' of candidate biomaterials for extrusion based 3D printing: state-of-the-art, Adv. Healthc. Mater. 6 (16) (2017).
[16] S. Raymond, Y. Maazouz, E.B. Montufar, R.A. Perez, B. Gonzalez, J. Konka, J. Kaiser, M.P. Ginebra, Accelerated hardening of nanotextured 3D-plotted self--setting calcium phosphate inks, Acta Biomater. 75 (2018) 451–462.
[17] L. Diaz-Gomez, M.E. Elizondo, P.D. Kontoyiannis, G.L. Koons, B. Dacunha-Marinho, X. Zhang, P. Ajayan, J.A. Jansen, A.J. Melchiorri, A.G. Mikos, Three-dimensional extrusion printing of porous scaffolds using storable ceramic inks, Tissue Eng. Part C: Methods 26 (6) (2020) 292–305.
[18] F. Seniha Güner, Y. Yağcı, A. Tuncer Erciyes, Polymers from triglyceride oils, Prog. Polym. Sci. 31 (7) (2006) 633–670.
[19] M.P. Ginebra, E. Fernandez, E.A. De Maeyer, R.M. Verbeeck, M.G. Boltong, J. Ginebra, F.C. Driessens, J.A. Planell, Setting reaction and hardening of an apatitic calcium phosphate cement, J. Dent Res. 76 (4) (1997) 905–912.
[20] D. Therriault, S.R. White, J.A. Lewis, Rheological behavior of fugitive organic inks for direct-write assembly, Appl. Rheol. 17 (1) (2007) 10112-1 –10112-8.
[21] A. Ribeiro, M.M. Blokzijl, R. Levato, C.W. Visser, M. Castilho, W.E. Hennink, T. Vermonden, J. Malda, Assessing bioink shape fidelity to aid material development in 3D bioprinting, Biofabrication 10 (1) (2017) 014102.
[22] M. Kesti, M. Müller, J. Becher, M. Schnabelrauch, M. D'Este, D. Eglin, M. Zenobi-Wong, A versatile bioink for three-dimensional printing of cellular scaffolds based on thermally and photo-triggered tandem gelation, Acta Biomater. 11 (2015) 162–172.
[23] H. Li, S. Liu, L. Li, Rheological study on 3D printability of alginate hydrogel and effect of graphene oxide, Int. J. Bioprinting 2 (2) (2016) 54–66.
[24] J.J. Senior, M.E. Cooke, L.M. Grover, A.M. Smith, Fabrication of complex hydrogel structures using suspended layer additive manufacturing (SLAM), Adv. Funct. Mater 29 (1904845) (2019) 1904845.
[25] L. Ouyang, R. Yao, Y. Zhao, W. Sun, Effect of bioink properties on printability and cell viability for 3D bioplotting of embryonic stem cells, Biofabrication 8 (2016) 035020.
[26] J.H.Y. Chung, S. Naficy, Z. Yue, R. Kapsa, A. Quigley, S.E. Moulton, G.G. Wallace, Bio-ink properties and printability for extrusion printing living cells, Biomater. Sci. 1 (2013) 763–773.
[27] X. Xu, A. Jagota, S. Peng, D. Luo, M. Wu, C.Y. Hui, Gravity and surface tension effects on the shape change of soft materials, Langmuir 29 (27) (2013) 8665–8674.
[28] A.T. Gaynor, J.K. Guest, Topology optimization considering overhang constraints: eliminating sacrificial support material in additive manufacturing through design, Struct. Multidisc. Optim. 54 (5) (2016) 1157–1172.
[29] A. Lode, K. Meissner, Y. Luo, F. Sonntag, S. Glorius, B. Nies, C. Vater, F. Despang, T. Hanke, M. Gelinsky, Fabrication of porous scaffolds by three-dimensional plotting of a pasty calcium phosphate bone cement under mild conditions, J. Tissue Eng. Regen. Med. 8 (9) (2014) 682–693.
[30] N. Raja, A. Sung, H. Park, H.S. Yun, Low-temperature fabrication of calcium deficient hydroxyapatite bone scaffold by optimization of 3D printing conditions, Ceram. Int. 47 (5) (2020) 7005–7016.
[31] A.R. Akkineni, Y. Luo, M. Schumacher, B. Nies, A. Lode, M. Gelinsky, 3D plotting of growth factor loaded calcium phosphate cement scaffolds, Acta Biomater. 27 (2015) 264–274.
[32] W. Zhang, C. Feng, G. Yang, G. Li, X. Ding, S. Wang, Y. Dou, Z. Zhang, J. Chang, C. Wu, X. Jiang, 3D-printed scaffolds with synergistic effect of hollow-pipe structure and bioactive ions for vascularized bone regeneration, Biomaterials 135 (2017) 85–95.
[33] Y. Luo, D. Zhai, Z. Huan, H. Zhu, L. Xia, J. Chang, C. Wu, Three-dimensional printing of hollow-struts-packed bioceramic scaffolds for bone regeneration, ACS Appl. Mater. Interfaces 7 (43) (2015) 24377–24383.
[34] L. Lei, Y. Wei, Z. Wang, J. Han, J. Sun, Y. Chen, X. Yang, Y. Wu, L. Chen, Z. Gou, Core–shell bioactive ceramic robocasting: tuning component distribution beneficial for highly efficient alveolar bone regeneration and repair, ACS Biomater. Sci. Eng. 6 (4) (2020) 2376–2387.
[35] T. Ahlfeld, N. Cubo-Mateo, S. Cometta, V. Guduric, C. Vater, A. Bernhardt, A.R. Akkineni, A. Lode, M. Gelinsky, A novel plasma-based bioink stimulates cell proliferation and differentiation in bioprinted, mineralized constructs, ACS Appl. Mater. Interfaces 12 (2020) 12557–12572.
[36] T. Ahlfeld, F.P. Schuster, Y. Förster, M. Quade, A.R. Akkineni, C. Rentsch, S. Rammelt, M. Gelinsky, A. Lode, 3D plotted biphasic bone scaffolds for growth factor delivery: biological characterization in vitro and in vivo, Adv. Healthcare Mater. 8 (2019) 1801512.
[37] R.F. Richter, T. Ahlfeld, M. Gelinsky, A. Lode, Development and characterization of composites consisting of calcium phosphate cements and mesoporous bioactive glass for extrusion-based fabrication, Materials 12 (2019) 2022.
[38] T. Ahlfeld, F. Doberenz, D. Kilian, C. Vater, P. Korn, G. Lauer, A. Lode, M. Gelinsky, Bioprinting of mineralized constructs utilizing multichannel plotting of a self-setting calcium phosphate cement and a cell-laden bioink, Biofabrication 10 (4) (2018) 045002.
[39] T. Hildebrand, A. Laib, R. Müller, J. Dequeker, P. Rüegsegger, Direct three-dimensional morphometric analysis of human cancellous bone: microstructural data from spine, femur, iliac crest, and calcaneus, J. Bone Mineral Res. 14 (1999) 1167–1174.
[40] E.F. Bertaut, Raies de Debye-Scherrer et Répartition des Dimensions des Domaines de Bragg dans les Poudres Polycristallines, Acta Cryst. 3 (1950) 14–18.
[41] M. Thommes, K. Kaneko, A.V. Neimark, J.P. Olivier, F. Rodriguez-Reinoso, J. Rouquerol, K.S. Sing, Physisorption of gases, with special reference to the evaluation of surface area and pore size distribution (IUPAC technical report), Pure Appl. Chem. 87 (9-10) (2015) 1051–1069.
[42] C. Canal, D. Pastorino, G. Mestres, P. Schuler, M.P Ginebra, Relevance of microstructure for the early antibiotic release of fresh and pre-set calcium phosphate cements, Acta biomater. 9 (9) (2013) 8403–8412.
[43] D. Pastorino, C. Canal, M.P. Ginebra, Multiple characterization study on porosity and pore structure of calcium phosphate cements, Acta biomater. 2015 (2015) 205–214.
[44] T. Ahlfeld, T. Köhler, C. Czichy, A. Lode, M. Gelinsky, A methylcellulose hydrogel as support for 3D plotting of complex shaped calcium phosphate scaffolds, Gels 4 (3) (2018) 68.
[45] E. Koos, N. Willenbacher, Capillary forces in suspension rheology, Science 331 (6019) (2011) 897–900.
[46] E. Koos, J. Johannsmeier, L. Schwebler, N. Willenbacher, Tuning suspension rheology using capillary forces, Soft Matter 8 (24) (2012) 6620.
[47] F.C.M Driessens, J.A. Planell, M.G. Boltong, I. Khairoun, M.P. Ginebra, Osteotransductive bone cements, Proc. Inst. Mech. Eng. H 212 (1998) 427–435.
[48] H. Noureddini, B.C. Teoh, L.D. Clements, Densities of vegetable oils and fatty acids, JAOCS 69 (1992) 1184–1188.
[49] H. Noureddini, B.C. Teoh, L.D. Clements, Viscosities of vegetable oils and fatty acids, JAOCS 69 (1992) 1189–1191.
[50] J. Zhang, W. Liu, V. Schnitzler, F. Tancret, J.M. Bouler, Calcium phosphate cements for bone substitution: chemistry, handling and mechanical properties, Acta Biomater. 10 (3) (2014) 1035–1049.
[51] S.V. Dorozhkin, Calcium orthophosphate-based biocomposites and hybrid biomaterials, J. Mater. Sci. 44 (9) (2009) 2343–2387.
[52] A.W.J.P Carrel, M. Moussa, P. Rieder, S. Scherrer, S. Durual, A 3D printed TCP/HA structure as a new osteoconductive scaffold for vertical bone augmentation, Clin. Oral. Implants Res. 27 (1) (2014) 55–62.
[53] J.P. Carrel, A. Wiskott, S. Scherrer, S. Durual, Large bone vertical augmentation using a three-dimensional printed TCP/HA bone graft: a pilot study in dog mandible, Clin. Implant Dentistry Relat. Res. 18 (6) (2016) 1183–1192.
[54] P. Korn, T. Ahlfeld, W. Pradel, A. Lode, A. Franke, M. Rauner, U. Range, B. Stadlinger, G. Lauer, M. Gelinsky, 3D-bioprinting of bone grafts for alveolar defects–a preclinical pilot study, Int. J. Oral Maxillofacial Surg. 48 (2019) 273.
[55] M. Gallo, S. Tadier, S. Meille, J. Chevalier, Resorption of calcium phosphate materials. Considerations on the in vitro evaluation, J. Eur. Ceram. Soc. 38 (3) (2018) 899–914.
[56] M. Bohner, Reactivity of calcium phosphate cements, J. Mater. Chem. 17 (38) (2007) 3980–3986.